*J. Fluid Mech.* (2008), *vol.* 609, *pp.* 305–317. © 2008 Cambridge University Press
doi:10.1017/S0022112008002164 Printed in the United Kingdom

# Stability of a stratified fluid with a vertically moving sidewall

FRANÇOIS BLANCHETTE[1], THOMAS PEACOCK[2] AND RÉMI COUSIN[2]

[1]Sch. Natural Sciences, University of California Merced, 5200 N. Lake Rd, Merced,
CA 95343, USA
[2]Dept. Mechanical Engineering, Massachusetts Institute of Technology, Cambridge,
MA 02139, USA

(Received 24 December 2007 and in revised form 16 April 2008)

We present the results of a combined theoretical and experimental study of the stability of a uniformly stratified fluid bounded by a sidewall moving vertically with constant velocity. This arrangement is perhaps the simplest in which boundary effects can drive instability and, potentially, layering in a stratified fluid. Our investigations reveal that for a given stratification and diffusivity of the stratifying agent, the sidewall boundary-layer flow becomes linearly unstable when the wall velocity exceeds a critical value. The onset of instability is clearly observed in the experiments, and there is good quantitative agreement with some predictions of the linear stability analysis.

## 1. Introduction

Flows in which vertical fluid motion induced at a sidewall is opposed by a stable ambient density stratification are present in a variety of geophysical and industrial systems (Turner 1985). Examples that have been studied in a laboratory setting include: heating or cooling of salt-stratifications (Thorpe 1969; Hart 1971; Huppert & Turner 1980); sidewall heating of polydisperse suspensions (Mendenhall & Mason, 1923); suspensions settling near an inclined wall in the presence of a density gradient (Peacock, Blanchette & Bush 2005); and double-diffusive systems in the presence of an inclined boundary (Linden & Weber 1977). A motivation for studying such a wide variety of mechanisms is their capacity to generate horizontal layers, which greatly influence mixing and transport.

Here, we concern ourselves with arguably the simplest mechanism by which instability can arise via sidewall forcing in a stratified system: a vertically-moving no-slip sidewall. In such a system, fluid is dragged vertically in a boundary layer adjacent to the moving sidewall, and this fluid motion is opposed by the ambient stratification. This scenario may arise in dip-coating processes, for example, where the thickness and uniformity of the coating-layer may be sensitive to conditions in the liquid bath (Weinstein & Ruschak 2004). The transient evolution in a stratified tank where an inclined sidewall is impulsively started was described by Standing (1971), and the related case of the stability near an oscillating vertical boundary in a stratified fluid has been investigated by Robinson & McEwan (1975); the present study may be considered as the zero-frequency limit of this regime.

In § 2, we obtain a solution for steady boundary-layer flow and discuss its characteristics. The stability analysis of this base flow profile is detailed in § 3, followed by the corresponding numerical results in § 4. Experimental details and

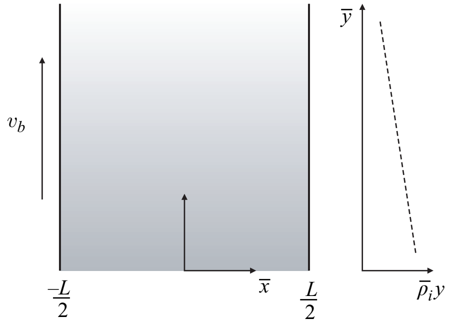

FIGURE 1. An infinitely tall container of width $L$ with a stationary sidewall at $\bar{x} = L/2$ and a sidewall moving vertically with velocity $v_b$ at $\bar{x} = -L/2$. In the absence of any sidewall motion a density stratification $\bar{\rho}_i(\bar{y})$ is present: $(\bar{x}, \bar{y})$ are the cartesian coordinates and $(\bar{u}, \bar{v})$ are the velocity components.

results are then presented in § 5, followed by a discussion and conclusions in §§ 6 and 7, respectively.

## 2. Steady flow

To model fluid motion for the configuration shown in figure 1, we use the Boussinesq approximation of the incompressible Navier–Stokes equations,

$$\nabla \cdot \boldsymbol{u} = 0, \qquad \frac{\mathrm{D}\boldsymbol{u}}{\mathrm{D}t} = -\frac{\nabla p}{\rho^*} + \nu \nabla^2 \boldsymbol{u} + \frac{\boldsymbol{g}\rho}{\rho^*}, \tag{2.1}$$

in combination with the density transport equation,

$$\frac{\mathrm{D}\rho}{\mathrm{D}t} = \kappa \nabla^2 \rho. \tag{2.2}$$

Here, $\boldsymbol{u} = (\bar{u}, \bar{v})$ is the $(\bar{x}, \bar{y})$ velocity vector, $p$ the pressure, $\nu$ the kinematic viscosity, $\rho$ the density, $\rho^*$ a representative density value, $\boldsymbol{g}$ the gravitational acceleration and $\kappa$ the diffusion coefficient of the stratifying agent. The boundary conditions are no-slip for the velocity at the sidewalls and no diffusive flux through the insulating sidewalls:

$$\boldsymbol{u}(-L/2, \bar{y}) = v_b \hat{y}, \qquad \boldsymbol{u}(L/2, \bar{y}) = 0, \qquad \partial_{\bar{x}} \rho(\pm L/2, \bar{y}) = 0, \tag{2.3}$$

where $\hat{y}$ is a unit vertical vector.

We non-dimensionalize equations (2.1) and (2.2) using the container thickness $L$ as a length scale, a diffusive time scale $L^2/\kappa$ and a typical density variation $L\mathrm{d}\bar{\rho}_i/\mathrm{d}\bar{y}$, where $\bar{\rho}_i(\bar{y})$ is the density stratification in the absence of sidewall motion. From this emerge the Rayleigh ($Ra$), Prandtl ($Pr$) and Péclet ($Pe$) numbers,

$$Ra = \frac{g\left(-\dfrac{1}{\rho^*}\dfrac{\mathrm{d}\bar{\rho}_i}{\mathrm{d}\bar{y}}\right)L^4}{\nu\kappa}, \qquad Pr = \frac{\nu}{\kappa}, \qquad Pe = \frac{v_b L}{\kappa},$$

which respectively distinguish the relative importance of buoyancy, viscosity and inertia compared to diffusion. Unless otherwise stated, henceforth all quantities are dimensionless.

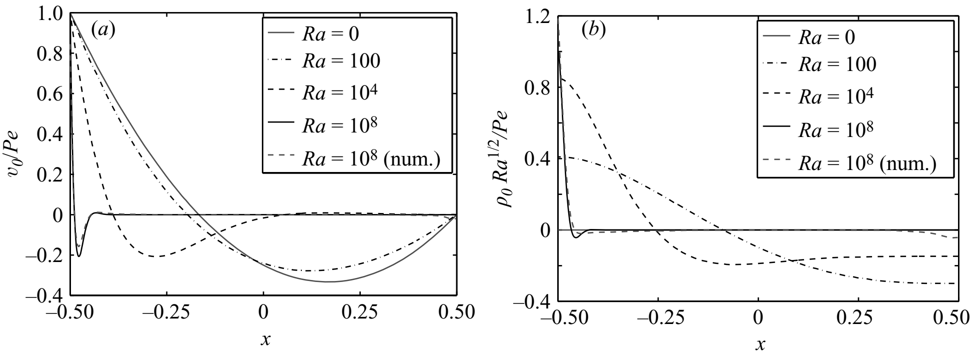

FIGURE 2. The steady vertical velocity profile $v_0$ (*a*) and corresponding density disturbance $\rho_0$ (*b*) for Rayleigh numbers ranging from 0 to $10^8$. The dashed grey curves were obtained via numerical simulations in a finite container.

We assume a steady unidirectional flow $(u, v) = (0, v_0(x))$, $p = p_0(y)$, and a steady density-profile comprising a constant gradient and a perturbation term, i.e. $\rho = -y + \rho_0(x)$. These assumptions implicitly require zero net vertical flux of fluid, which is perhaps the most relevant scenario for comparison with experiments in a finite-sized container. The resulting system of equations is linear in the velocity and density, and we therefore eliminate the density to obtain the governing steady-state equation

$$\partial_{xxxx} v_0 + Ra\, v_0 = 0, \tag{2.4}$$

with boundary conditions

$$v_0\left(-\tfrac{1}{2}\right) = Pe, \quad v_0\left(\tfrac{1}{2}\right) = 0, \quad Ra\,\partial_x \rho_0\left(\pm\tfrac{1}{2}\right) = \partial_{xxx} v_0\left(\pm\tfrac{1}{2}\right) = 0. \tag{2.5}$$

The general solution of (2.4) is

$$\begin{aligned} v_0(x) = {}& \mathrm{e}^{x\sqrt{2}/d}\left(c_1 \cos\left(\frac{x\sqrt{2}}{d}\right) + c_2 \sin\left(\frac{x\sqrt{2}}{d}\right)\right) \\ & + \mathrm{e}^{-x\sqrt{2}/d}\left(c_3 \cos\left(\frac{x\sqrt{2}}{d}\right) + c_4 \sin\left(\frac{x\sqrt{2}}{d}\right)\right), \end{aligned} \tag{2.6}$$

where $d = Ra^{-1/4}$ is the boundary-layer thickness and the coefficients $c_i$ are set by the boundary conditions (2.5). The density is then found by solving $v_0 = -(\rho_0)_{xx}$.

Examples of velocity and density profiles for four different Rayleigh numbers covering the range $Ra = 0$ to $Ra = 10^8$ are shown in figures 2(*a*) and 2(*b*) respectively. These profiles are found to agree with the long-time limit of the transient solution obtained by Standing (1971). In the limit of vanishing background stratification, and thus vanishing Rayleigh number, the requirement of a steady density profile enforces a parabolic velocity profile with zero net volume-flux. The density profile at low Rayleigh number shows a nearly antisymmetric perturbation, with an increase near the moving boundary resulting from a balance of vertical advection and diffusion. In the limit of large Rayleigh number, both the fluid motion and density variation become confined to a boundary layer of thickness $d$. We can rationalize the thickness of the boundary layer for steady flow by simultaneously balancing vertical advection of density with horizontal diffusion, and buoyancy forces with viscous dissipation:

$$v_b \frac{\mathrm{d}\bar{\rho}_i}{\mathrm{d}\bar{y}} \sim \kappa \frac{\Delta\rho}{\bar{d}^2}, \qquad g\Delta\rho \sim \rho\nu \frac{v_b}{\bar{d}^2}, \tag{2.7}$$

where $\Delta\rho$ is an undetermined horizontal density variation across the boundary layer. This simple scaling analysis reveals that $\bar{d} = Ld = LRa^{-1/4}$, a result consistent with the analytical result (2.6). The time scale to establish this flow is set by the viscous and diffusive time scales across the boundary layer, which are $\bar{d}^2/\nu$ and $\bar{d}^2/\kappa$, respectively.

We investigated the influence of the right-hand wall by replacing the stationary boundary condition at $x = 1/2$ with a downward velocity $v = -Pe$, and solving for a steady flow. This yields a linear velocity profile in the limit of $Ra \to 0$, also with zero net volume-flux. For $Ra \geqslant 10^4$, the boundary-layer profile becomes nearly identical to the case of a stationary sidewall at $x = 1/2$. Since the experiments described in § 5 were conducted at high Rayleigh number ($Ra \sim 10^{12}$), we reasonably expect that the stability of our system will not be affected by the boundary condition at the right-hand wall. We also verified that the finite vertical extent of a container does not significantly affect the boundary layer flow, provided the container is much larger than the boundary layer. To confirm this we performed numerical simulations of a container with equal height and width, at $Ra = 10^8$. Except in boundary-layer regions adjacent to the upper and lower boundaries of the container, the velocity and density profiles were found to closely match the theoretical profile (2.6), as shown in figure 2.

## 3. Linear stability analysis

The boundary-layer flow induced by a moving sidewall will be unstable when a random horizontally displaced perturbation, of typical size $\bar{d}$ and density difference $\Delta\rho$, accelerates sufficiently before diffusion can re-establish the steady-state profile. Balancing the buoyancy of the perturbation with viscous forces yields a settling time scale $t_s \sim \rho\nu/\bar{d}g\Delta\rho \sim \bar{d}/v_b$; while the diffusive time scale is $t_d \sim \bar{d}^2/\kappa \sim Pr^{1/2}/N$, where $N = (g(1/\rho^*)\mathrm{d}\bar{\rho}_i/\mathrm{d}y)^{1/2}$ is the Brunt–Väisälä frequency. A simple scaling analysis therefore predicts that instability occurs when $t_d > t_s$, and thus

$$v_b > \kappa/\bar{d}. \tag{3.1}$$

We therefore anticipate that the critical wall velocity for instability will depend only on the diffusion constant and boundary layer thickness.

Using the methods described by Finlayson (1972) and following Paliwal & Chen (1979), we consider perturbations of the steady state (2.6). We introduce a streamfunction $\psi$ such that $\partial_x\psi = -v$ and $\partial_y\psi = u$, and consider the perturbed state $\psi = \psi_0 + \psi'$ with corresponding density $\rho = \rho_0 + \rho'$. Assuming perturbations of the form

$$\psi' = \psi'(x)\exp(\mathrm{i}\alpha y + \sigma t), \qquad \rho' = \rho'(x)\exp(\mathrm{i}\alpha y + \sigma t), \tag{3.2}$$

we obtain the linearized system:

$$\begin{aligned} 0 = -\frac{\sigma}{Pr}(\partial_{xx}\psi' - \alpha^2\psi') - \frac{\mathrm{i}\alpha}{Pr}(v_0(\partial_{xx}\psi' - \alpha^2\psi') - \psi'\partial_{xx}v_0) \\ + (\partial_{xxxx}\psi' - 2\alpha^2\partial_{xx}\psi' + \alpha^4\psi') - Ra\ \partial_x\rho', \end{aligned} \tag{3.3}$$

$$0 = -\sigma\rho' + (\partial_{xx}\rho' - \alpha^2\rho') + \mathrm{i}\alpha\psi'\partial_x\rho_0 - \mathrm{i}\alpha v_0\rho' + \partial_x\psi'. \tag{3.4}$$

The boundary conditions on the perturbations are no-slip and no density flux:

$$\psi' = \partial_x\psi' = \partial_x\rho' = 0 \qquad \text{at } x = \pm\tfrac{1}{2}. \tag{3.5}$$

We note that perturbations in the third dimension (depth) may also arise, but as a first step toward understanding the stability of this system we proceed with the two-dimensional analysis.

We solve the eigenvalue problem (3.3)–(3.4) and determine for which values of $\alpha$, $Pe$, $Pr$ and $Ra$ the real part of $\sigma$, Re($\sigma$), is positive, corresponding to growing instabilities. To do so, we first expand the perturbations in a series of functions of a known form:

$$\psi'(x)=\sum_{n=1}^{\infty} a_n\psi^n(x), \qquad \rho'(x)=\sum_{n=1}^{\infty} b_n\rho^n(x),$$

where the functions $\psi^n(x)$ and $\rho^n(x)$ are chosen to satisfy the homogeneous boundary conditions (3.5), to obey an eigenvalue problem of the form $\partial_{xxxx}\psi=\lambda\psi$, and to form complete orthogonal sets. The functions $\rho^n$ are sines and cosines, while the $\psi^n$ are combinations of hyperbolic and trigonometric functions, both with frequencies increasing with $n$. The Galerkin method is used to project equations (3.3) and (3.4) onto the basis functions $\psi^n$ and $\rho^n$, respectively, each equation being integrated from $x=-1/2$ to $x=1/2$ to yield an algebraic equation for the coefficients $a_n$ and $b_n$. To solve for these coefficients we truncate the infinite system, keeping only the first $N$ terms. Thus, we obtain a system of equations of the form $(A-\sigma B)x=0$, where $x$ is a vector containing the coefficients $a_n$ and $b_n$. To find unstable, non-trivial solutions, we solve for eigenvalues, $\sigma$, with Re($\sigma$) > 0.

## 4. Numerical results

We consider Rayleigh numbers in the range $10^3$–$10^8$ for two different Prandtl numbers, corresponding to salt-water ($Pr=600$) and heat-water ($Pr=7$) systems. For given Rayleigh and Prandtl numbers we have calculated the critical Péclet number, $Pe_c$, above which the system is unstable. The number of basis functions used, $N$, always exceeded 24, and care was taken to verify that the results did not vary by more than 1 % as $N$ was further increased; larger values of $Ra$ required $N$ as large as 72. The numerous integrals resulting from the projection of the basis functions onto themselves were also evaluated numerically, and again the degree of accuracy was verified to have a less than 1 % effect on the results. Moreover, results obtained using the density and velocity profiles obtained numerically in a finite container changed the computed $Pe_c$ by only 4 %.

A critical Péclet number above which instabilities develop exists for the entire range of $Ra$ considered, as shown in figure 3(*a*). For $Ra\leqslant 10^3$ and $Pr=7$, $Pe_c$ is on the order of $10^4$ or larger, in which case finite-amplitude shear-induced instabilities are possible as the Reynolds number ($Re=Pe/Pr$) is greater than $10^3$; such instabilities are not detected by a linear stability analysis (Grossmann 2000). As $Ra$ increases, a minimum value of $Pe_c\approx 800$ is reached at $Ra\approx 80\,000$ for both Prandtl numbers before rising again with increasing Rayleigh number (note that figure 3*a* shows $Pe_c/Ra^{1/4}$, rather than $Pe_c$). There are some abrupt changes in $Pe_c$ for $Ra\leqslant 10^4$, which are associated with different eigenmodes becoming unstable. These are manifest as corresponding abrupt variations of the instability frequency, Im($\sigma_c$), and the critical wavelength, $\alpha_c$, in figures 3(*b*) and 3(*c*), respectively. Such behaviour is not uncommon; double-diffusive systems, for example, exhibit non-monotonically varying critical numbers as the most-unstable mode varies with the Rayleigh number (Thangam, Zebib & Chen 1981). Despite the sharp change in wavenumber and frequency, however, there is little variation in the horizontal form of the different

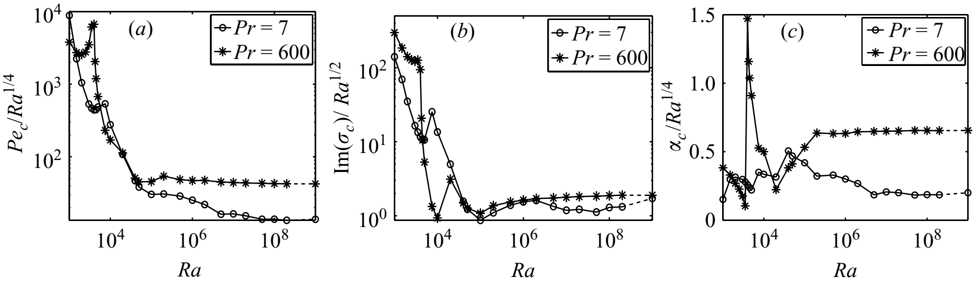

FIGURE 3. Dependence on the Rayleigh number of (*a*) the critical Péclet number, $Pe_c$, (*b*) the oscillation frequency $\mathrm{Im}(\sigma_c)$ and (*c*) the wavenumber, $\alpha_c$, of the most-unstable mode. All plots show results obtained for heat-water ($Pr = 7$) and salt-water ($Pr = 600$) systems. Points on the far right were obtained in the limit $Ra \to \infty$ as described in § 6.

eigenfunctions. As $Ra$ increases above $10^5$, $Pe_c$ increases as $Ra^{1/4}$. In this limit, the stability of the system is independent of the tube width $L$, as motion is confined to a thin boundary layer near the wall and is unaffected by the presence of a far away boundary.

The variation of $\mathrm{Im}(\sigma_c)$ with $Ra$ is presented in figure 3(*b*). This quantity is always positive, and the instability is therefore a travelling wave propagating in the opposite direction to the moving boundary. As the Rayleigh number becomes large, $\mathrm{Im}(\sigma_c)$ scales as $Ra^{1/2}$; the frequency of instability is therefore $\kappa/\bar{d}^2$. The most-unstable wavelength at the onset of instability, $\alpha_c$ is plotted as a function of $Ra$ in figure 3(*c*). For $Ra > 10^5$, $\alpha_c$ scales as $Ra^{-1/4}$ and the multiplicative factor relating them is order 1 for both Prandtl numbers. The scale of the instability is thus on the order of the boundary layer thickness.

The numerical results show that for $Ra > 10^5$ the relevant length scale to consider is not the tank width $L$ but the boundary-layer width $\bar{d}$. We therefore consider the limit $L/\bar{d} \to \infty$, in which the previously defined Rayleigh number also tends to infinity. Non-dimensionalizing the governing equations using $\bar{d}$ rather than $L$, the Rayleigh and Péclet numbers are $Ra_\infty = 1$ and $Pe_\infty = v_b \bar{d}/\kappa$. In this limit, a critical Péclet number exists for $7 \leqslant Pr \leqslant 600$. When $Pr > 100$, the critical Péclet number for instability is $Pe_{\infty c} \approx 43$, and the critical boundary velocity is therefore

$$v_b \approx 43\kappa/\bar{d}, \tag{4.1}$$

consistent with the prediction of our scaling argument (3.1). The corresponding critical wavenumber is $\alpha_{\infty c} \approx 0.65$, giving a critical wavelength

$$\lambda_c = (2\pi/\alpha_c)\bar{d} \approx (2\pi/0.65)\bar{d} \approx 9.4\bar{d}. \tag{4.2}$$

The frequency of the most unstable mode is $\omega_c = \mathrm{Im}(\sigma_{\infty c}) \approx 1.9$, corresponding to a period

$$T = (2\pi/1.9)\bar{d}^{\,2}/\kappa \approx 3.3\bar{d}^{\,2}/\kappa. \tag{4.3}$$

For $Pr = 7$, appropriate to heat-water systems, $Pe_{\infty c} \approx 14$, and $\alpha_{\infty c} \approx 0.2$, while $\mathrm{Im}(\sigma_{\infty c})$ is essentially unchanged. We note that these results repeat the scaling obtained for $10^5 < Ra < 10^8$, in which case it can reasonably be assumed that this behaviour persists in the range $10^8 < Ra < \infty$.

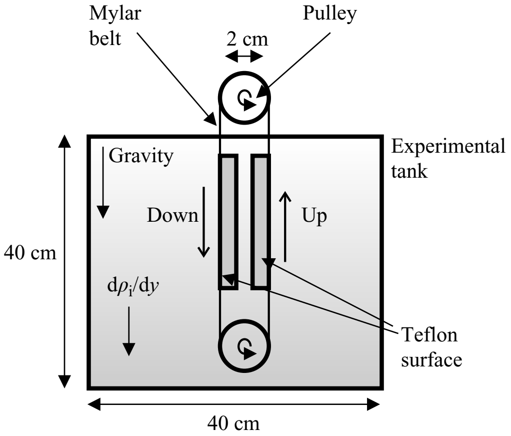

FIGURE 4. Schematic of the experimental apparatus. A thin Mylar conveyer-belt, kept taught by two Teflon-coated surfaces, is mounted on a pair of rollers. The top roller is driven by a microstepper motor and the consequent vertical motion of the Mylar belt generates an adjacent boundary-layer flow in the ambient stratification. The onset of instability for this flow is studied using Synthetic Schlieren.

## 5. Experiments

### 5.1. *Apparatus*

A schematic of the experimental arrangement is shown in figure 4. An acrylic tank 40 cm high with a 40 cm × 30 cm base was filled with linearly stratified salt-water using the double-bucket method (Oster 1965). The density gradient, measured using both density floats and selective withdrawal, covered the range $-23\,\mathrm{kg\,m^{-4}}$ to $-517\,\mathrm{kg\,m^{-4}}$. Vertically-moving sidewalls were achieved using a thin 28.5-cm-wide Mylar conveyor-belt standing vertically in the middle of the tank. To isolate it both mechanically and thermally from the surroundings, the Mylar conveyor-belt was looped around two rubber rollers. The outside of the conveyor-belt was open to the stratification, whereas the inside lay flat against Teflon-coated surfaces, which kept the conveyor-belt taught whilst allowing smooth motion. The motion of the Mylar belt, which was upwards in one half of the tank and downwards in the other, was driven by a microstepper motor. Belt velocities were set in the range $0.50\text{–}2.60 \pm 0.01\,\mathrm{mm\,s^{-1}}$, and both the magnitude and steadiness of this motion were verified by analysing movies of the belt motion taken using a CCD camera. The water temperature was constant throughout the tank to within 0.2 °C.

The onset of instability was detected using the Synthetic Schlieren technique (Sutherland *et al.* 1999). A random pattern of dots backlit by a uniform light sheet was placed 30 cm behind the back wall of the tank. A 50-mm-square region of the random pattern that contained both the up and down moving walls was viewed horizontally through the tank using a 1024 × 1264 pixel CCD camera, positioned 3 m from the front wall of the tank. Instability of the boundary-layer flow adjacent to the conveyor-belt generated perturbations of the density gradient field (and thus refractive-index gradient field), which in turn produced apparent distortions of images of the random pattern that could be detected using the software Digiflow. A cross-correlation search window of 19 × 19 pixels with 3-pixel overlap gave an experimental resolution of 0.75 mm, with apparent displacements of 0.04 mm (1 pixel) readily detectable. In each case, the reference image used for the Synthetic Schlieren processing was obtained

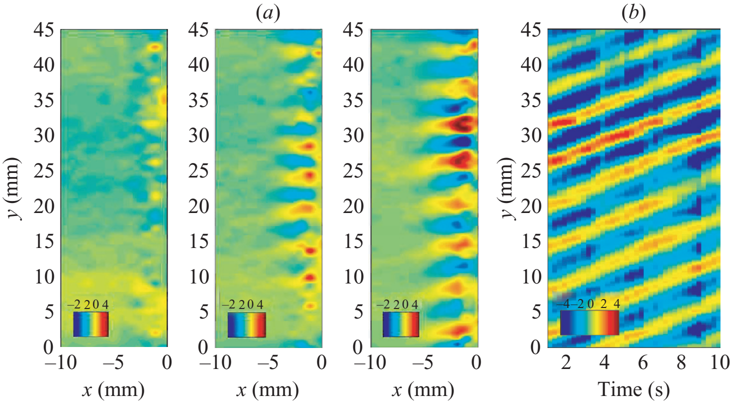

FIGURE 5. (*a*) Perturbations adjacent to the downward-moving boundary, which is on the right-hand side of each image at $x = 0$, for a background stratification of $-274\,\mathrm{kg\,m^{-4}}$ ($Ra = 2.2 \times 10^{12}$). Wall velocities are $1.34\,\mathrm{mm\,s^{-1}}$ (left), $1.49\,\mathrm{mm\,s^{-1}}$ (centre) and $1.55\,\mathrm{mm\,s^{-1}}$ (right), corresponding to $Pe = 1.68, 1.86$ and $1.94\ \times 10^5$, respectively. (*b*) Time series of the vertical density-gradient perturbation for a wall velocity of $1.55\,\mathrm{mm\,s^{-1}}$ obtained using a vertical cut at $x = -2.5$ mm. The colourmap indicates the amplitude of the perturbation to the ambient vertical density gradient in $\mathrm{kg\,m^{-4}}$.

with the steady-state flow present, as the optical distortions generated by the steady-state flow distorted the view of the original mask so strongly as to prevent successful cross-correlation.

In a typical experiment, a stratification was established and the conveyor-belt set in motion at a velocity well below the onset of instability. In this regime, a vertically uniform optical distortion could be observed very close (∼1 mm) to the moving walls, corresponding to the unidirectional boundary layer. The velocity of the conveyor-belt was then increased in steps of $0.05\,\mathrm{mm\,s^{-1}}$ and the system was left to stand for 10 minutes after each adjustment, to allow reasonable time for an instability to initiate and spread across the width of the moving boundary. Several trial experiments were left running for much longer between adjustments (∼1 hour) without any change in the results. This process was repeated until an instability, which was manifest as a spatially periodic structure, could be recognized. The onset of instability was then checked for hysteresis by increasing the conveyor-belt velocity to $0.3\,\mathrm{mm\,s^{-1}}$ above critical and systematically reducing the velocity in steps of $0.05\,\mathrm{mm\,s^{-1}}$. No evidence of hysteresis could be found, and the same critical value was determined whether the critical velocity was approached from above or below. The experiments were repeated for a range of stratifications, and in several cases repeated months later (which required rebuilding the experiment from scratch), to confirm repeatability, and to study some aspects of the instability in more detail.

### 5.2. *Results*

A typical set of experimental images showing the transition from a stable to an unstable boundary-layer flow, obtained using a background stratification of $-274\,\mathrm{kg\,m^{-4}}$, is presented in figure 5. For these images, the belt, located on the right-hand side of the image, is moving downwards, and the sidewall of the experimental tank is far (>150 mm) beyond the left-hand border. The vertical extent of the images presented in figure 5 is 4.5 cm, which was located at the midheight of the tank. A few small perturbations are visible in the immediate vicinity of the boundary in

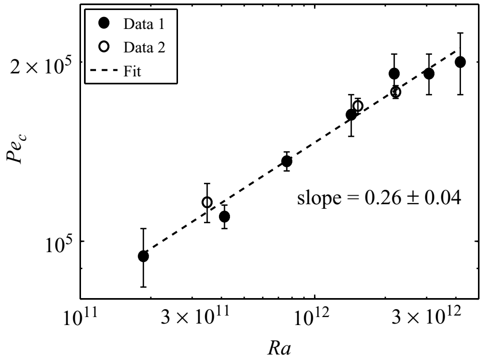

FIGURE 6. Experimental data for the onset of instability, plotted as $\log_{10}(Pe_c)$ vs $\log_{10}(Ra)$. A best-fit line of slope 0.26 is drawn through the data. The results labelled 'Data 2' were taken several months after 'Data 1'.

the left-hand image, for which $v_b = 1.34\,\mathrm{mm\,s^{-1}}$. These perturbations displayed no coherence over time periods even as short as one quarter of a second, however, and were therefore considered to be noise. For $v_b = 1.49\,\mathrm{mm\,s^{-1}}$, the first clear evidence of instability emerged, as demonstrated by the middle image of figure 5(*a*). A periodic structure can readily be observed, and the wavelength was determined from several such images taken at different times to be $4.7 \pm 0.2$ mm. The characteristic density gradient perturbation was $3\,\mathrm{kg\,m^{-4}}$, on the order of 1 % of the background stratification. Above this critical wall velocity, the periodic structure became even more apparent. This is evident in the right-most image of figure 5(*a*), for which $v_b = 1.55\,\mathrm{mm\,s^{-1}}$. The perturbations are noticeably stronger at this supercritical wall velocity, and the wavelength has increased to $5.3 \pm 0.4$ mm. The periodic structure extends several millimetres from the moving boundary into the ambient, and this did not noticeably change if left for several hours, implying that nonlinear effects were saturating its growth. We confirmed that the behaviour of the system was the same throughout the central 20 cm of the tank. There was no evidence of any end effects as cells evolved uniformly across the entire domain of investigation (as opposed to obvious sequential growth from the top or bottom) and appeared simultaneously on both the upward and downwards moving walls.

The periodic structure was not stationary at onset, but travelled in the opposite direction to the adjacent moving boundary. This is demonstrated by the image in figure 5(*b*), which was generated by plotting the temporal evolution of the density-gradient perturbation for a vertical cut at $x = -2.5$ mm in the right-most image of figure 5(*a*). The periodic structure moves upwards, in the direction opposite to that of the neighbouring boundary which is moving downwards. The frequency of the instability was $0.21 \pm 0.1$ Hz at onset (which was close to the natural buoyancy frequency of 0.26 Hz for this experiment) and did not change noticeably as $v_b$ was increased through the critical value. The phenomenon was mirrored in the other half of the experimental tank, where the instability had the same wavelength and moved downwards with the same velocity adjacent to the upwards moving wall.

We determined the critical wall velocity at the onset of instability for a range of linear stratifications, and the results are presented in figure 6, in which we plot the critical Péclet number, $Pe_c$, as a function of the Rayleigh number, *Ra* (based on the half-width of our experimental tank). The results were highly repeatable, as demonstrated by the second set of data points (Data 2), which were taken several months after the first experimental results (Data 1). A best-fit line to the data in this log–log plot gives a slope of $0.26 \pm 0.04$, agreeing with the $\frac{1}{4}$ power scaling predicted by the linear stability analysis. For the repeated experiments (Data 2), we carefully measured the wavelength and frequency of the instability at onset. The wavelengths were $\lambda_a = 7.6 \pm 0.3$ mm and $\lambda_b = 4.7 \pm 0.2$ mm for density gradients of $-43\,\mathrm{kg\,m^{-4}}$ and $-274\,\mathrm{kg\,m^{-4}}$, respectively; and the frequencies at onset were $\omega_a = 0.09$ Hz and $\omega_b = 0.21$ Hz, respectively. These values agree well with the predicted scaling of the instability wavelength: $\lambda_a/\lambda_b = 1.62$ compared to $(43/274)^{-1/4} = 1.59$; and $\omega_a/\omega_b = 0.43$ compared to $(43/274)^{1/2} = 0.40$.

No coherent macroscale layer structure was ever observed to develop. Once the instability appeared at the critical wall velocity it soon became saturated, and never extended beyond a few millimetres into the ambient, even if the critical wall velocity was maintained for several hours. Nor was there any clear evidence of splitting or merging of the observed periodic structure as the wall velocity was increased above critical. Rather, the spatially periodic structure became increasingly incoherent and intermittent. Some larger-scale features, perhaps a secondary instability, were observed to develop and decay within the boundary layer, but not in any organized manner.

## 6. Discussion

Our experiments clearly identify the onset of an instability in a density stratified fluid due to a vertically moving sidewall. Consistent with the predictions of linear theory, $Pe_c$ scales as $Ra^{\frac{1}{4}}$, $\alpha_c$ scales as $Ra^{-\frac{1}{4}}$, and at onset the instability is oscillatory and propagates in the opposite direction to the adjacent moving boundary with a frequency $\mathrm{Im}(\sigma_c)$ that scales as $Ra^{\frac{1}{2}}$.

Whilst the scalings for the physical quantities measured are the same, the absolute values, are different. Linear theory predicts $Pe_c \approx C_1 Ra^{1/4}$, with $C_1 \approx 43$, whereas experimental data yield $C_1 \approx 127$. The critical wall velocities detected in the experiment were therefore nearly 3 times larger than those predicted. Linear theory also predicts $\alpha_c \approx 9.4\bar{d}$, which, using $\nu = 10^{-6}\,\mathrm{m^2\,s^{-1}}$ and $\kappa = 1.5 \times 10^{-9}\,\mathrm{m^2\,s^{-1}}$, corresponds to 1.2–2.7 mm for our experiments. We measured the instability wavelength to be significantly larger; for example, 7.6 mm for a density gradient of $-43\,\mathrm{kg\,m^{-4}}$. Finally, the observed frequency was significantly higher than that predicted (and close to the natural buoyancy frequency of the stratification); for example, 0.21 Hz compared to the predicted value of 0.02 Hz for a density gradient of $-274\,\mathrm{kg\,m^{-4}}$.

A possible reason for the disagreement between experiment and theory is that the experimental apparatus was simply not sensitive enough to record the true onset of instability. Our experimental arrangement, however, could reliably detect perturbations that were less than 1 % of the background stratification for the strongest density gradients, and it is difficult to envisage readily improving upon this. The resolution of our experiment, 0.75 mm, was comparable to the predicted wavelength. To verify that indeed our resolution was sufficient, we performed test experiments with the camera more closely zoomed in, increasing the resolution to 0.25 mm at the expense of a slightly weaker optical signal. This made no difference to our results. To ensure that we were allowing sufficient time for an instability to develop, we left the system running for several hours in weakly subcritical states, but no periodic structure evolved.

To further understand the discrepancy between experiment and theory, we numerically investigated the instability as $Pe$ is increased above the critical value. We considered the limit $L/\bar{d} \to \infty$, which is the regime of the experiments. Figure 7(*a*)

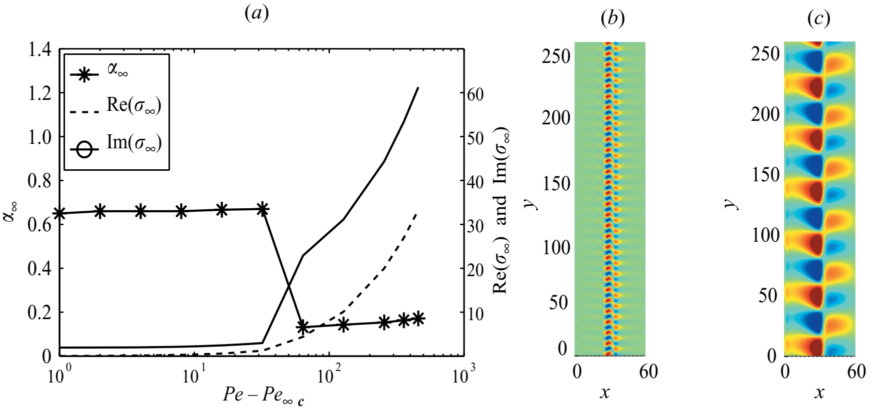

FIGURE 7. (*a*) Most-unstable wavenumber, $\alpha_\infty$, and growth rate of the instability, $\sigma_\infty$, for Péclet numbers exceeding the critical value computed through linear stability analysis, $Pe_{\infty c} = 43$. Computations were performed in the infinite Rayleigh number limit and with $Pr = 600$. Results are non-dimensionalized with the boundary-layer thickness $L \sim \bar{d}$ and the diffusive time scale $t \sim \bar{d}^2/\kappa$. (*b*) and (*c*) Density perturbation eigenmodes for $\alpha = 0.68$ and $\alpha = 0.14$, respectively, at $Pe_\infty = 110$. Lengths are expressed in terms of $\bar{d}$ and the computational domain had width $60\bar{d}$.

shows the dependence, in this limit, of the most-unstable wavenumber, $\alpha_\infty$, growth rate of the instability, $\mathrm{Re}(\sigma_\infty)$, and oscillation frequency, $\mathrm{Im}(\sigma_\infty)$, on the Péclet number. When $Pe_\infty = v_b\bar{d}/\kappa$ exceeds the critical value by approximately 50, the most-unstable wavenumber decreases sharply to 0.14. Moreover, the growth rate of the instability increases by an order of magnitude, and the oscillation frequency also increases, albeit more smoothly. The theoretical critical Péclet number corresponding to this second instability is approximately 95, compared to an observed value of 127. The predicted wavelengths are approximately 10.4 mm and 6.6 mm for density gradients of $-43\,\mathrm{kg\,m^{-4}}$ and $-274\,\mathrm{kg\,m^{-4}}$, respectively, which compare favourably with our observed values of 7.6 mm and 4.3 mm. Finally, the theoretical oscillation frequency becomes 0.11 Hz and 0.25 Hz, respectively, also in good agreement with our observations of 0.09 Hz and 0.21 Hz.

To gain further insight, we also investigated the spatial structure of these linear instabilities to see if this could distinguish which mode was excited. The density perturbations for eigenmodes with wavenumbers $\alpha = 0.68$, and $\alpha = 0.14$ in the limit of $L/\bar{d} \to \infty$ are presented in figures 7(*b*) and 7(*c*), respectively. In contrast to our experimental observations, both eigenmodes display large variations near the centre of domain, and bear little resemblance to the observed structures in figure 5(*a*). It is noteworthy that the eigenmode corresponding to $\alpha = 0.14$, figure 7(*c*), shows a local maximum near $x = 2\bar{d}$, in contrast to the eigenmode $\alpha = 0.68$ which shows no horizontal structure of a scale comparable to that of the boundary layer.

One possibility, therefore, is that we observed a manifestation of the larger-scale stronger instability that occurs when $Pe - Pe_{\infty c} > 50$, as it is more conducive to experimental observation evolving on a time scale of minutes rather than tens of minutes or hours, and therefore being more robust in the face of experimental noise. The horizontal structure of the instability we observed, however, was not determined by a linear instability, which suggests that nonlinear effects, which are largest near the boundary layer, or perhaps three-dimensionality, play an important role in determining the structure of the instability.

## 7. Conclusion

We have demonstrated that an instability occurs if a vertical sidewall bounding a stratified fluid is moved up or down with sufficient velocity. In the experiments, conducted using a salt-water stratification, scalings predicted by linear theory for the critical wall velocity, wavelength and frequency of the instability as a function of the background stratification were reliably reproduced. Although the absolute values of these parameters were larger than predicted, the level of agreement obtained is reasonable given the inherent limitations of linear theory, and is comparable to that obtained for the onset of instability in analogous double-diffusive systems (Tanny & Tsinober 1988; Kerr 2000). No macroscale layering was observed to result from the detected instability.

In conclusion, we note that the physical arrangement we have studied corresponds to vertical Couette flow between parallel plates (Dauchot & Daviaud 1995). The analysis predicts that for a 10-cm-wide system, a vertical temperature gradient as small as $0.05\,^{\circ}\mathrm{C\,m^{-1}}$ would have a critical Péclet number of $Pe_c \approx 1000$. The corresponding Reynolds number, $v_b L/\nu = Re \approx 150$, would then be below the threshold for nonlinear instabilities associated with the transition to turbulence. The very small scale of the instability may mean it would go unnoticed, but still provide finite-amplitude perturbations capable of triggering nonlinear instabilities.

We would like to acknowledge the financial support of the MIT-France program.

## REFERENCES

Dauchot, O. & Daviaud, F. 1995 Finite-amplitude perturbation and spots growth-mechanism in plane couette-flow. *Phys. Fluids* **7**, 335–343.

Finlayson, B. A. 1972 *The Method of Weighted Residuals and Variational Principles*, pp. 151–203. Academic.

Grossmann, S. 2000 The onset of sheer flow turbulence. *Rev. Mod. Phys.* **72** (2), 603–618.

Hart, J. E. 1971 Sideways diffusive instability. *J. Fluid Mech.* **49**, 279–288.

Huppert, H. E. & Turner, J. S. 1980 Ice blocks melting into a salinity gradient. *J. Fluid Mech.* **100**, 167–384.

Kerr, O. S. 2000 The criteria for the onset of double-diffusive instabilities at a vertical boundary. *Phys. Fluids* **12** (12), 3289–3292.

Linden, P. & Weber, F. 1977 The formation of layers in a double-diffusive system with a sloping boundary. *J. Fluid Mech.* **81**, 757–773.

Mendenhall, C. E. & Mason, M. 1923 The stratified subsidence of fine particles. *Proc. Natl Acad. Sci.* **9**, 199–202.

Oster, G. 1965 Density gradients. *Sci. Am.* **213**, 70.

Paliwal, R. C. & Chen, C. F. 1979 Double-diffusive instability in an inclined fluid layer. Part 2. stability analysis. *J. Fluid Mech.* **98**, 769–785.

Peacock, T., Blanchette, F. & Bush, J. W. M. 2005 The stratified Boycott effect. *J. Fluid Mech.* **529**, 33–49.

Robinson, R. M. & McEwan, A. D. 1975 Instability of a periodic boundary-layer in a stratified fluid. *J. Fluid Mech.* **68**, 41.

Standing, R. G. 1971 The rayleigh problem for a slightly diffusive density-stratified fluid. *J. Fluid Mech.* **48**, 673–688.

Sutherland, B. R., Dalziel, S. B., Hughes, G. O. & Linden, P. F. 1999 Visualisation and measurement of internal waves by ‘synthetic schlieren’. Part 1. Vertically oscillating cylinder. *J. Fluid Mech.* **390**, 93–126.

Tanny, J. & Tsinober, A. B. 1988 The dynamics and structure of double-diffusive layers in sidewall heating experiments. *J. Fluid Mech.* **196**, 151–160.

Thangam, S., Zebib, A. & Chen, C. F. 1981 Transition fronmm shear to sideways diffusive instability in s vertical slot. *J. Fluid Mech.* **112**, 151–160.

Thorpe, S. A. 1969 The effect of horizontal gradients on thermohaline convection. *J. Fluid Mech.* **38**, 375–400.

Turner, J. S. 1985 Multicomponent convection. *Annu. Rev. Fluid. Mech.* **17**, 11–44.

Weistein, S. J. & Ruschak, K. J. 2004 Coating rows. *Annu. Rev. Fluid Mech.* **36**, 29–53.